ACS APPLIED MATERIALS & INTERFACES

Research Article

www.acsami.org

Intercalation Anode Material for Lithium Ion Battery Based on Molybdenum Dioxide

Uttam Kumar Sen, Apoorv Shaligram, and Sagar Mitra*

Electrochemical Energy Laboratory, Department of Energy Science and Engineering, Indian Institute of Technology Bombay, Powai, Mumbai-400076, India

Supporting Information

ABSTRACT: MoO_2 is one of the most studied anode systems in lithium ion batteries. Previously, the reaction of MoO_2 with lithium via conversion reaction has been widely studied. The present study highlights the possible application of MoO_2 as an intercalation-based anode material to improve the safety of lithium ion batteries. Nanobelts of MoO_2 are prepared by reduction of MoO_3 nanobelts under hydrogen atmosphere. The intercalation behavior of MoO_2 is specially focused upon by limiting the charge−discharge cycling to narrow potential window of 1.0 to 2.2 V vs Li/Li^+ to avoid conversion reaction. An excellent electrochemical stability over 200 cycles is achieved at a current rate of 100 mAh g^{-1}. A phase transformation from monoclinic to orthorhombic to monoclinic is observed during the lithiation process, which is reversible during delithiation process and is confirmed by ex-situ XRD and electrochemical impedance spectroscopy. To further demonstrate the viability of MoO_2 as a commercial anode material, MoO_2 is tested in a full-cell configuration against $LiFePO_4$. The full-cell assembly is cycled for 100 cycles and stable performance is observed. The combination showed an energy density of 70 Wh kg^{-1} after 100 cycles.

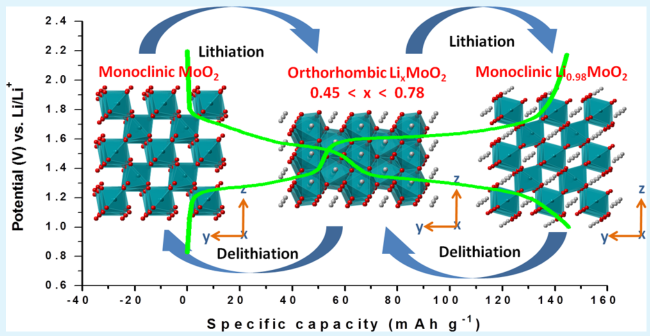

KEYWORDS: *lithium ion battery, intercalation anode, $LiFePO_4$, MoO_2, nanobelt morphology*

INTRODUCTION

Since the commercialization of lithium ion batteries (LIBs), intercalation-based electrode materials have dominated the anode electrochemistry. A graphite-based anode is always preferred in terms of cost and cycle life, but at the same time, it suffers from operational safety and charge performance which is of utmost importance to next-generations battery applications like electric vehicles.[1,2] In this context, high-performance anodes based on metal oxide materials have been investigated.[3,4] Metal oxide-based anodes can easily be grouped into two subgroups. One class is intercalation-based material that works at relatively high potential (1.4−1.8 V vs Li/Li^+) with low lithium intake capacity.[5−7] On the other hand, the second class of material belongs to the more popular conversion-based mechanism that can store a maximum amount of lithium per transition metal atom and exhibit satisfactory rate performance at relatively low potential ∼0.6−0.8 V vs Li/Li^+).[3,8,9] However, such conversion-based metal oxides have not gained much industrial interest because of inherent problems associated with large polarization loss and huge volume change, which leads to capacity fading.[8,10]

In recent time, oxide-based intercalated anode host matrices have gained much interest because of high volumetric energy density, safety, and high power performance in charging cycle over graphite, all of which are important parameters in electric vehicle application. In this context, lithium titanate ($Li_4Ti_5O_{12}$) becomes the most attractive and successful anode material for lithium ion batteries due to zero strain effect during lithium intercalation and fewer safety issues.[6,11] Recently, a $Li_{1+x}V_{1-x}O_2$-based intercalated anode was studied by Armstrong et al.[12] and they showed the low potential intercalation phenomena of lithium (∼0.1 V vs Li/Li^+) and it could be considered as an alternative to a graphite anode. The main problems associated with such a vanadium-based electrode are toxicity and high electronic resistivity associated with the material. Like graphite, these anode candidates also have an operating potential close to that of lithium metal, and thus, the safety concern regarding accidental lithium plating due to high current/low temperature charging arises in all such materials.

Furthermore, in the literature, efforts have been made to increase energy storage capacity and rate performance of various metal oxide-based anodes. The molybdenum oxide-based anode is one of the most studied systems in recent time due to its spectacular electrochemistry associated with molybdenum, high electrochemical activity toward lithium, and high electrical conductivity.[13,14] Molybdenum forms two binary oxides, MoO_3 and MoO_2. Among them, the more attractive MoO_3 phase holds widespread interests in the fields

Received: June 7, 2014
Accepted: July 25, 2014
Published: July 25, 2014

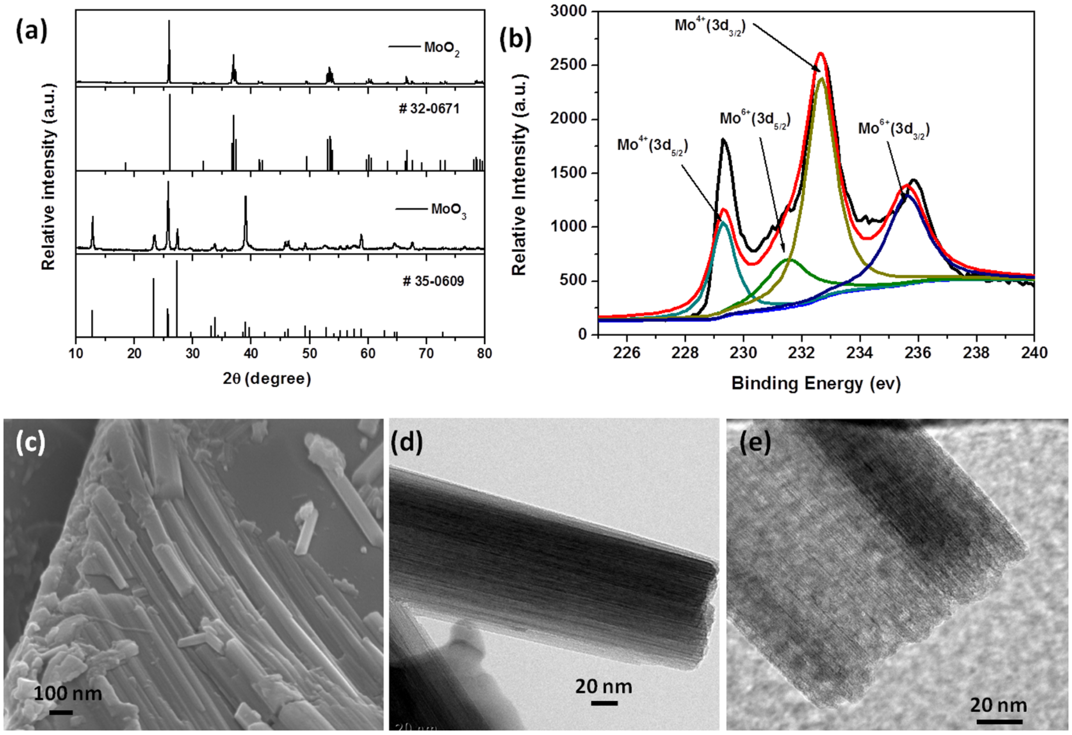

Figure 1. (a) X-ray diffraction (XRD) pattern of MoO_2 and MoO_3 along with standard JCPDS data, (b) deconvoluted core level spectra of Mo 3d from high-resolution X-ray photoelectron spectroscopy (XPS) spectra of MoO_2 sample, (c) FEG-SEM image of MoO_2 sample, and (d and e) FEG-TEM images of MoO_2 nanobelts at two different magnifications.

of heterogeneous catalysis,[15] electrochromic and photochromic devices,[16] mechanical logic gate development,[17] gas sensing,[18] and as a possible host material for Li intercalation in Li ion batteries.[19] More interestingly, MoO_3 can be reduced to form six stable Magnéli phases, leading to the lower stable oxide MoO_2.[20,21] As per reports, MoO_2 crystallizes in a monoclinic structure (space group $P21/c$) and the structure is closely related to the distorted rutile structure.[22] The MoO_2 phase is less important in technological applications than MoO_3, but it has been used as a promising anode material for Li ion batteries recently.[14,23−29] In most of the cases, it was considered as a conversion-based anode and exhibited high energy density. However, most of the reports were unsuccessful in making an impact in literature due to its poor electrochemical performance compared to other conversion-based oxides.[14,24,27,29]

Dahn et al.[7] were the first to report the intercalation behavior of MoO_2 host. However, not much research has been done on similar lines. Prior to this report, no focused attempts have been made toward the use of MoO_2 as intercalation-based anode materials for LIBs. In this study, monoclinic MoO_2 was prepared by reducing MoO_3 in hydrogen atmosphere and used as an intercalation anode in the potential window from 1.0 to 2.2 V vs Li/Li^+. We selected this material to study the lithium intercalation mechanism and to demonstrate the feasibility of such an anode as a successful electrode material in a half-cell configuration against Li as well as in a full-cell configuration against the commercial $LiFePO_4$ cathode. The charge−discharge behavior was explained with the help of ex-situ XRD and continuous electrochemical impedance spectroscopy. It is also noteworthy to mention here that in addition to lithium ion battery characterization, we have studied the physical and morphological behavior of material in detail.

■ EXPERIMENTAL SECTION

Molybdenum dioxide (MoO_2) was prepared by a two-step synthesis process. In first step, molybdenum trioxide was prepared by a hydrothermal synthesis method.[19] The as-prepared MoO_3 was then reduced in reducing atmosphere at 650 °C. In a typical synthesis process, 2.0 g of sodium molybdate ($Na_2MoO_4{\cdot}2H_2O$, Merck) was dissolved in 10 mL of deionized water followed by controlled acidification using 5 mL of 4 N perchloric acid ($HClO_4$, Merck). The solution was then transferred into a 35 mL Teflon-lined stainless steel autoclave and heated at 180 °C for 24 h. The white precipitation obtained at the end of the reaction was washed with deionized water several times and finally dried at 60 °C for 12 h in a hot air oven. The as-prepared white-colored MoO_3 powder was taken in a quartz boat and then placed inside a tubular furnace at 650 °C for 4 h in a mixture of H_2/N_2 gas flow (5% H_2 + 95% N_2). After 4 h of heating, the system was cooled to room temperature under a constant flow of 5% H_2. A grayish powder was obtained, which was used for further study.

Materials Characterization. The as-prepared powder samples were characterized by powder X-ray diffraction (XRD) measurements using a Philips X′-pert diffractometer equipped with Cu Kα radiation (λ = 1.5418 Å). Elemental analysis was performed with X-ray photoelectron spectroscopy measurements in a Thermo VG Scientific photoelectron spectrometer (MultiLab) equipped with an Al Kα source (1486.6 eV). Peak fitting and analysis were done using XPS peak 4.1 software. XPS analysis was done on the electrode surface (MoO_2 along with carbon and binder on Cu foil). The surface morphology of the powder sample was studied by a field emission gun scanning electron microscope (FEG-SEM, JEOL-7600F) having a resolution of ∼1 nm. Further microstructure investigation was carried out using a high-resolution field emission gun transmission electron microscope (HR-TEM, JEOL-2100F). The electron diffraction patterns obtained from TEM analysis were indexed using SingleCrystal software (CrystalMaker Software Ltd.), whereas the measurements on TEM image were done using an ImageJ tool.

Cell Fabrication and Electrochemical Measurements. Galvanostatic charge−discharge of the half-cell configuration was carried out in CR2032 coin cells. The cells were assembled inside an argon-filled glovebox (Lab Star, MBRAUN) with controlled moisture and an oxygen level of ~1 ppm. A thin layer of metallic lithium pasted on the stainless steel disk was used as counter as well as reference electrode. Borosilicate glass microfiber filters (GF/D Whatman) soaked in 1 M $LiPF_6$ in EC/DMC (1:1 weight ratio) (LP-30, Merck) electrolyte were used as a separator. The MoO_2 anode was prepared using as-prepared MoO_2 powder as active material, carbon black (Super C-65, Timcal, Switzerland) as conductive additive, and polyvinylidene difluoride (PVDF) as polymeric binder in 80:12:08 weight ratio. A homogenous, thick slurry was prepared using *N*-methylpyrrolidone (NMP) as solvent. The slurry was cast on a Cu metal foil and dried in vacuum oven for 12 h at 120 °C. Cyclic voltammetry (CV) experiments were performed by measuring *i*−*V* response at a scan rate of 0.1 mV s^{-1} within a potential limit of 2.2−1.0 V vs Li/Li^+ using a Biologic VMP-3 model. The electrochemical charge−discharge tests were performed using an Arbin Instrument (BT2000 model) at various current rates within a voltage cutoff of 2.2 and 1.0 V vs Li/Li^+. Electrochemical impedance spectroscopy (EIS) was carried out at different potentials during the charge−discharge process using the Biologic VMP-3 instrument. During the entire process, the cell was not disconnected from the circuit, and we termed this technique as in situ impedance spectroscopy or continuous impedance spectroscopy. Five different potential points were selected for EIS measurements, such as open circuit voltage and 1.5 and 1.0 V vs Li/Li^+ during the discharge process and at 1.6 and 2.2 V vs Li/Li^+ during the charge process. At each point, potentiostatic EIS was taken within a frequency range from 1 MHz to 0.1 Hz and with voltage amplitude of ΔV = 5 mV. For EIS experiments, charge−discharge was carried out at a constant current density of 20 mA g^{-1}. All the electrochemical measurements were done at a constant temperature of 20 °C with controlled humidity.

The full-cell characterizations were performed using CR2016 type coin cells in the configuration of $LiFePO_4$/electrolyte/MoO_2, and 1 M $LiPF_6$ in 1:1 EC:DMC (w/w) (LP-30, Merck) was used. A 20 μm thick, 40% porous polyethylene (PE) membrane was used as a separator. $LiFePO_4$ cathode was prepared by using commercial-grade $LiFePO_4$ as active material (LinYi Gelon LIB Co. Ltd.), SuperC65-grade carbon as conductive additive, and PVDF as binder in a ratio of 70:20:10 by weight.

For ex-situ characterization, charge−discharge cycles were done in Swagelok-type cells, as they can be opened and reused. Electrodes were charged and discharged at a slower rate of 20 mA g^{-1}. The cell was stopped at the desire potential and was immediately opened inside an argon-filled glovebox, and the thin film electrodes were washed with diethyl carbonate (DEC) to remove electrolyte and finally dried at 60 °C under vacuum for 12 h inside the glovebox.

■ RESULTS AND DISCUSSION

Material Characterization. The crystallinity and purity of the powder sample obtained by the reduction process (both before and after reduction) were determined by XRD (shown in Figure 1a). X-ray diffraction pattern indicates that MoO_3 was completely reduced to MoO_2 after reduction in hydrogen atmosphere at 650 °C. The diffraction pattern can be readily indexed to monoclinic MoO_2 with a space group of *P*21/*c*, in good agreement with the JCPDS card no. 32-0671. The high indexed diffraction peaks located at 26.0°, 37.0°, and 53.6° (2θ) are attributed to the ($\bar{1}$11), ($\bar{2}$11), and ($\bar{2}$22) reflection planes of MoO_2 (JCPDS card no. 32-0671). The observed sharp peaks indicate the high crystallinity of the monoclinic MoO_2 material that we have obtained from the reduction process. More interestingly, the diffraction peaks corresponding to MoO_3 phase are not observed, which indicates the complete conversion of MoO_3 into MoO_2 phase.

Further, X-ray photoelectron spectroscopy (XPS) experiments have been performed, and the obtained results confirm the reduction of Mo from VI to IV oxidation state in the sample. The survey spectrum (Figure S1, Supporting Information) of the MoO_2 sample shows distinct signals at 232.7, 397.6, 417.0, and 530.4 eV, which are assigned to the Mo 3d, $3p_{3/2}$, and $3p_{1/2}$ and O 1s respectively, indicating the contributions from MoO_2.[26,28] The Mo 3d peak was examined by high-resolution XPS, shown in Figure 1b. The Mo $3d_{5/2}$ peak is centered at 229.3 eV, whereas the Mo $3d_{3/2}$ peak is found at 232.6 eV, with a spin energy separation of 3.3 eV. This characteristic doublet of core-level Mo $3d_{5/2}$, $3d_{3/2}$ indicates the Mo(IV) oxidation state of MoO_2. In addition, higher energy, low intensity peaks [in comparison to Mo(IV) peaks] at 231.5 and 235.6 eV originated from Mo(VI) $3d_{5/2}$ and $3d_{3/2}$ of MoO_3. The peak positions for Mo(IV) and Mo(VI) agree well with the reported values for MoO_2.[26,28,30] MoO_3 formation occurs due to the slight surface oxidation of MoO_2 in air.

FEG-SEM and FEG-TEM techniques were used to add further insight into the morphological and textural details of the MoO_2 sample, as shown in Figure 1c−e. A beltlike morphology was observed with a belt width of around 50−60 nm, whereas the length observed is in the micrometer range. It is quite interesting to note that the morphology of the MoO_3 (Figure S2 in Supporting Information) was retained after reduction to MoO_2. Further analysis shows that each belt consists of several nanosheets. Figure 2b,c clearly shows that the nanosheets were stacked one upon another to form the belts. Sometimes there is a little displacement during stacking, which was reflected during electron diffraction (Figure 2d,e).

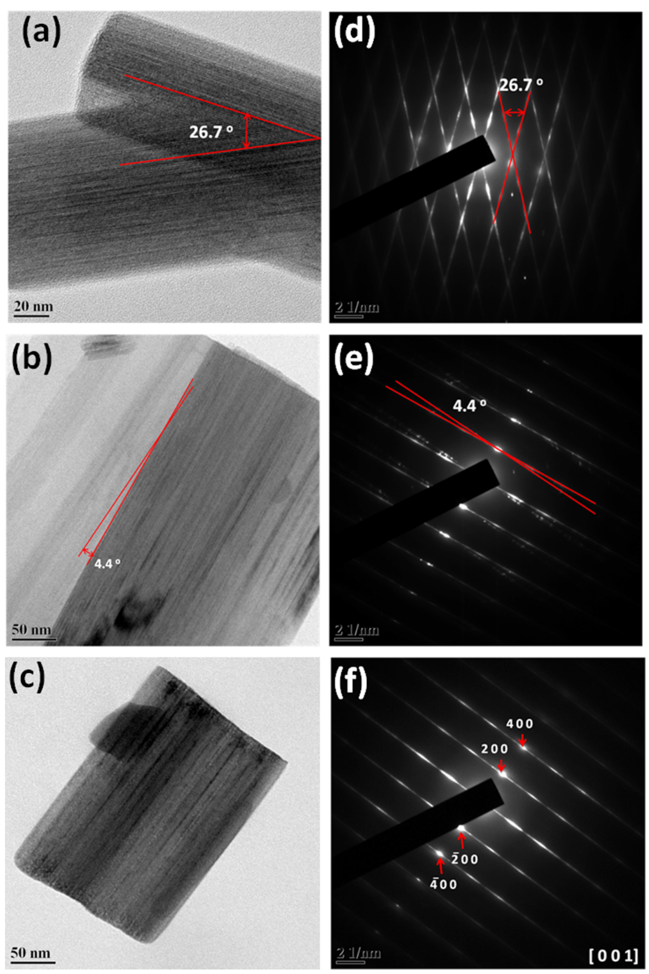

Figure 2. TEM Image of MoO_2 nanobelts (a−c) and their corresponding SAED pattern (d−f) in different lattice orientations.

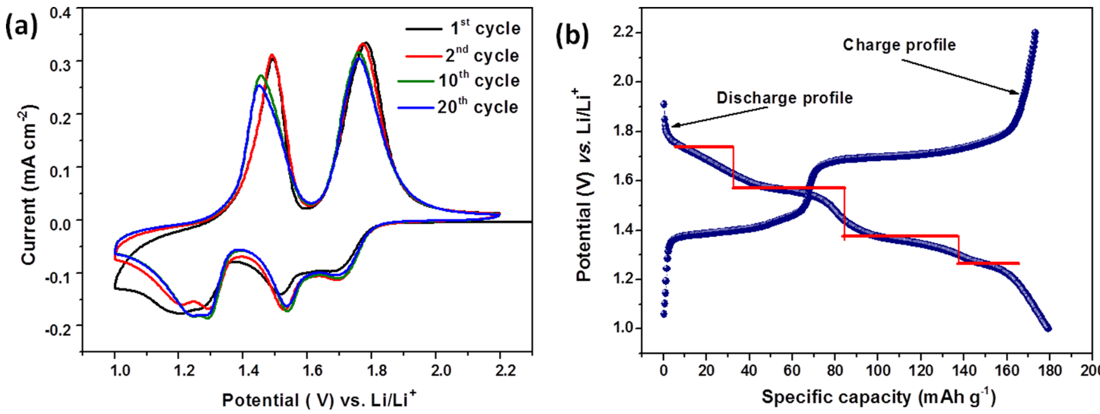

Figure 3. (a) Cyclic voltammetry at 0.1 mV s^{-1} and (b) second cycle charge−discharge profile at 20 mA g^{-1} for the MoO_2 electrode within the potential range of 2.2−1.0 V vs Li/Li^+.

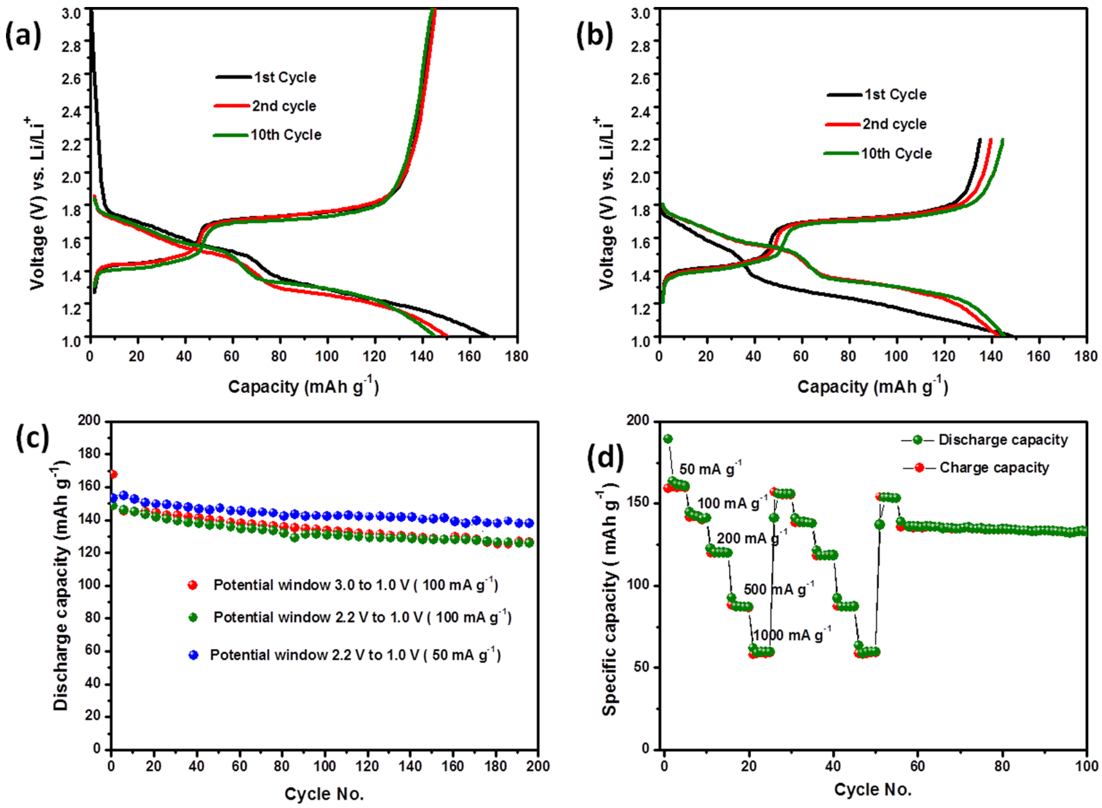

Figure 4. The charge−discharge profile of MoO_2 electrode within the potential range of (a) 3.0−1.0 V and (b) 2.2−1.0 V, (c) cyclic performance at different rates, and (d) power capability test for the MoO_2 anode. (Note: part c is plotted for every five points.)

A high-magnification image of the nanobelts of MoO_2 (Figure 2) shows the belt to be largely composed of elongated sheetlike shapes. FEG-TEM images also show the displacement in nanosheets stacking to form nanobelts. The angles of displacements were also measured from the corresponding selected area electron diffraction (SAED) pattern. The SAED pattern was indexed as the monoclinic phase of MoO_2.

Electrochemical Performance. MoO_2 can accommodate lithium ions in the tunnels of the monoclinic structure via intercalation mechanism. A four-step lithium intercalation was observed during the discharge process of MoO_2 electrode. Our primary interest in this material was to investigate the intercalation mechanism of this material rather than conversion reaction. In the previous reports, efforts have been only employed to use MoO_2 as a conversion anode by cycling within the potential window from 3.0 to 0.01 V vs Li/Li^+, which achieves a specific capacity within the range of 600−800 mAh g^{-1} with a decent cyclic stability.[26−28] However, the intercalation capability of this material is not yet explored in a practical scenario. Monoclinic MoO_2 can theoretically accommodate up to one Li atom via intercalation reaction,[7] leading to a capacity contribution of ∼209 mAh g^{-1}.

To investigate this mechanism, cyclic voltammetry was recorded at a scan rate of 0.1 mV s^{-1} within the potential window from 2.2 to 1.0 V vs Li/Li^+, as displayed in Figure 3a. Four prominent peaks were observed at 1.71, 1.53, 1.30, and 1.21 V vs Li/Li^+ during the cathodic sweep. The four reduction peaks were associated with four steps of the lithium insertion reaction into the monoclinic structure of MoO_2. Figure 3b shows four plateaus during the discharge process of MoO_2 when cycled at a slow discharge rate of 20 mA g^{-1}. It was proposed that a multistep phase transformation (monoclinic to orthorhombic to monoclinic) of Li_xMoO_2 occurred during the lithium insertion and extraction process.[7] A similar kind of four-step lithium insertion mechanism was previously observed in other monoclinic structures such as $NH_4V_4O_{10}$.[31] On the other hand, two sharp peaks at 1.49 and 1.77 V vs Li/Li^+ were observed in the reverse anodic sweep. The peak at 1.49 V is attributed to the phase transformation from monoclinic structure to orthorhombic phase, whereas at 1.77 V another phase transformation occurs, which is orthorhombic to monoclinic phase.

Furthermore, the MoO_2 anode was cycled in galvanostatic mode against metallic Li in a potential window from 2.2 to 1.0 V vs Li/Li^+, unlike literature reports where it was cycled within 3.0−0.01 V. It was observed that for the MoO_2 electrode, the Li intercalation reaction occurred above 1.0 V vs Li/Li^+, whereas other reactions like the conversion reaction, solid electrolyte interface (SEI) formation, and electrolyte decomposition are predominant below 1.0 V. These unwanted side reactions were the main reason behind the electrochemical destabilization of MoO_2 electrode. During this study, the MoO_2 anode was cycled up to 1.0 V vs Li/Li^+, and it was observed that during the charge process there is no further capacity addition beyond 2.2 V. Therefore, all the electrochemical studies were performed within the potential window of 2.2−1.0 V vs Li/Li^+. A comparison of voltage cutoff is shown in Figure 4a−c that shows that there is no significant difference in capacity addition on charging beyond 2.2 V. It has been observed that the MoO_2 anode exhibits a good cycling performance. Reversible discharge capacities of 139 and 126 mAh g^{-1} were achieved after 200 cycles for the MoO_2 electrode at a specific current rate of 50 and 100 mA g^{-1} respectively. The minimal capacity loss in the initial cycles suggest that the irreversible processes such as the decomposition of the electrolyte molecules are minimal, which justifies the use of a smaller potential window. The Coulombic efficiency of these three electrodes is shown in Figure S3 (Supporting Information). It can be observed that the excellent Coulombic efficiency was observed for normal charge−discharge performance. At the end of 150 cycles, more than 99% Coulombic efficiency was recorded. Higher Coulombic efficiency was observed for a narrow potential window charge−discharge process. The cycling performance of the MoO_2 electrode material at different current densities is shown in Figure 4d. Power cycle performance also shows the highly robust nature of the electrode.

The progress of the reaction was investigated by the use of ex-situ XRD analysis and continuous electrochemical impedance spectroscopy (EIS) methods. Ex-situ XRD analysis shown in Figure 5 depicts the XRD pattern of MoO_2 electrode before cycling at open circuit voltage (OCV), at 1.5 V in discharge (middle of the discharge reaction), at 1.0 V in discharge (end of discharge process), at 1.6 V in charge (middle of charge process), at 2.2 V (end of first complete cycle), and after the second complete cycle. It was observed that during the discharge process, some extra peaks at 21.2°, 24.95°, 26.81°, 27.61°, 30.81°, and 33.21° (marked in blue arrow) were observed at a cutoff voltage of 1.5 V. The presence of these extra peaks confirms the evolution of orthorhombic phase[24] at the middle of the reaction. On further progress, the orthorhombic peaks were observed to be diminished,

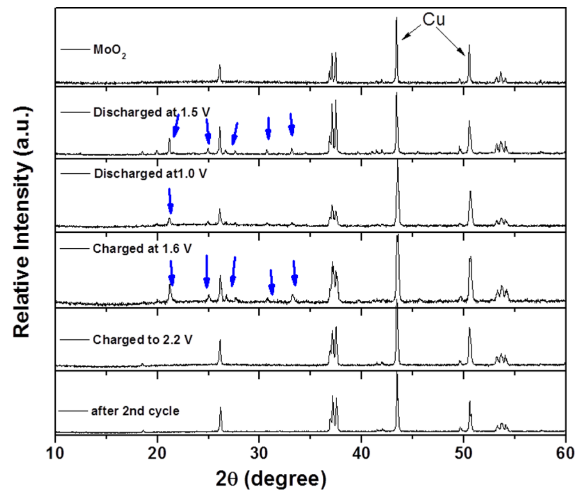

Figure 5. Ex-situ X-ray diffraction pattern of MoO_2 electrode at different potentials during a constant current charge−discharge cycling experiment.

confirming the phase transformation from orthorhombic to monoclinic. Similarly during the charge process, the monoclinic phase transformed to an orthorhombic phase at 1.6 V and then completely converted to a monoclinic phase upon full removal of Li at 2.2 V. The XRD pattern of the fully charged anode resembles that of the electrode before cycling, which again signifies that MoO_2 can fully transverse back to its initial phase, and it is true for the next cycle as well.

The corresponding electrochemical impedance spectroscopy (EIS) was carried out to understand the electrode behavior during lithiation and delithiation processes in the MoO_2 electrode. In-situ (or continuous) EIS analysis was done on the MoO_2 electrode (shown in Figure 6). EIS was taken during the charge−discharge process at specified potentials. Five different potentials along with the charge−discharge profile are shown in Figure 6c. In an ideal scenario, impedance spectra should contain three major time constants: a high-frequency semicircle related to the surface films ($R_{\text{Li ion migration}}$; some author also call this R_{SEI}) which is coupled with non-Faradic parts such as film capacitance, a medium-frequency semicircle related to charge transfer resistance R_{ct} coupled with interfacial capacitance, and a straight line with an inclination known as the Warburg element that relates to the solid-state Li ion diffusion into the bulk of the active material.[32,33] But in several cases, the high- and medium-frequency region semicircles were so close in time scale so that they overlapped each other and became indistinguishable, forming a single semicircle.[34−38] It should also be noted that the EIS measurements were done on a two-electrode system, whereas a three-electrode cell was emphasized for EIS measurements so that no current should flow between the working and the reference electrodes and the response is only obtained from the working electrode.[33,35]

In the present case, one semicircle followed by an inclined straight line is observed for all the impedance spectra, except at the fully lithiated state. The high-frequency semicircle is mainly contributed from charge transfer resistance (R_{CT}) and constant phase element (CPE), and the straight line (W) is from the diffusion of charged species through the bulk of the electrode material. The equivalent circuit drawn for this system is shown in Figure 6e, where R_1 represents the electrolyte resistance or the solution resistance of the electrochemical cell, whereas R_2 and Q_2 are designated as the electronic resistance of the

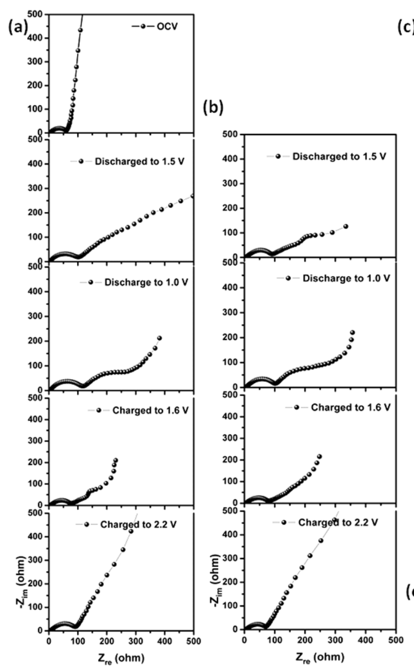

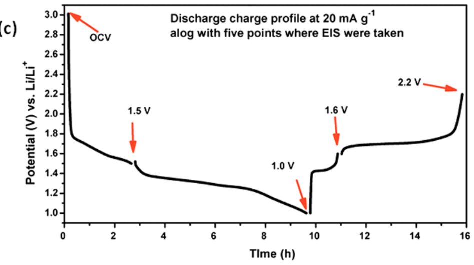

(d)

Potentials	R_1	R_2	R_3
OCV	5.46	60.28	-
1.5 V (half discharge)	5.13	86.16	
1.0 V (full discharge)	5.46	102.8	112.9
1.6 V (half charge)	5.70	69.19	
2.2 V (full charge)	5.53	92.92	

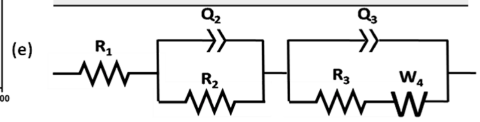

Figure 6. EIS spectra at different potentials during (a) the first and (b) the second charge−discharge cycling, (c) charge−discharge profile of the first cycle along with potential points where EIS spectra were taken, (d) tabulation of impedance values of the first charge−discharge cycle, and (e) equivalent circuit of the electrochemical process happening in the half-cell configuration (Randles circuit).

material and the associated capacity, which includes the constant phase angle element (accounting for the rough nature of the electrode),[39−41] respectively. The second semicircle only appeared at the fully lithiated electrode. The diffusion-controlled Warburg resistance is represented by W_4. The impedance values obtained from EIS analysis are tabulated in Figure 6d. It was observed that the electrolyte resistance, i.e., R_1 value, was almost identical for all the EIS measurements, which again implies that the contribution from the electrolyte resistance is independent of charge−discharge behavior. On the other hand, R_2, which is mostly associated with surface phenomenon, increases upon the lithiation process. The increase of R_2 value from 60 to 102 Ω indicates that, along with surface passivation, some resistive interfaces were also developed. Phase transformation of MoO_2 from monoclinic to orthorhombic also contributes to an increase in resistance value. At the end of the discharge process, a resistive interface was formed, which leads to an increase in the charge transfer resistance among different phases. The formation of another semicircle with a resistance value of ∼112 Ω (R_3) is associated with the bulk electronic resistance of the material. On the other hand, upon the delithiation process, the impedance profile slightly changes mainly in the low-frequency region, whereas the high-frequency region remains unaffected. Upon further delithiation, a single semicircle was observed and that is identical to the impedance profile obtained at the OCV point, although the R_2 value was increased from 60 Ω (at OCV) to 93 Ω (at 2.2 V). The experiments were repeated for the second cycle, which shows behavior identical with that of the first cycle.

Full-Cell Study. A full-cell performance has been demonstrated using MoO_2 as anode and commercial $LiFePO_4$ as cathode material. Details of the cell fabrication have been discussed in the Experimental Section. A cathode-limited cell performance is displayed in Figure 7. As we know, in half-cell assembly, metallic Li acts as a reservoir for Li ions, whereas in the full-cell configuration, cathode $LiFePO_4$ is the only source for Li ions; therefore, capacity balance is necessary to complete utilization of electrode material during cycling. The capacity balance is cathode-limited to ensure that there is no failure due to lithium plating. Figure 7 displays the electrochemical performance of all full cells comprised of a $LiFePO_4$/LP-30/MoO_2 assembly tested between 1.5 and 2.2 V at 20 °C. The full cell was initially charged and discharged at C/10 rate for 10 cycles and then at C/5 for the remaining 90 cycles within the voltage ranges of 2.2−1.5 V. Unlike the open structure of the borosilicate separator, the tortuous nature of the polymer separator may add to the cell resistance. The effect of cell polarization is may be magnified due to this in a full cell and may lead to an increase in the observed charging voltage. To avoid loss of cell capacity due to a lower cutoff voltage, in the initial three cycles, the cell was charged up to 2.6 V. After three cycles, this value was reduced to 2.2 V, as it was observed that there was no significant electrochemical activity beyond this value. Another reason for reducing the charge cutoff value was to prevent/reduce any unwanted side reactions or degradation of electrolyte, as that could possibly affect the overall cycling performance of the cell. Figure 7a shows a specific discharged capacity of 130 mAh g^{-1} at C/10, which is 87% of the practical capacity of the commercial $LiFePO_4$ (150 mAh g^{-1} at C/10). Figure 7b shows that there was a first cycle irreversible capacity loss of about 30 mAh g^{-1}. After 10 cycles, a capacity fade of 40 mAh g^{-1} was observed, out of which 30 mAh g^{-1} irreversible loss can be attributed to the first cycle. So, a minimal loss of 10 mAh g^{-1} was observed over 10 cycles, which suggests the good electrochemical stability of the electrode. The plateaus seen in Figure 7b show the characteristic of MoO_2 half-cell plateaus. Charge plateaus of a full cell, corresponding to discharge plateaus of the MoO_2 half-cell, are seen around 1.9 and 2.1 V. Figure 7c,d shows the half-cell charge and discharge performance of MoO_2 and $LiFePO_4$ and the expected voltage profile of a full cell constructed with the two materials. Figure 7e,f shows the comparison between expected (calculated) and observed

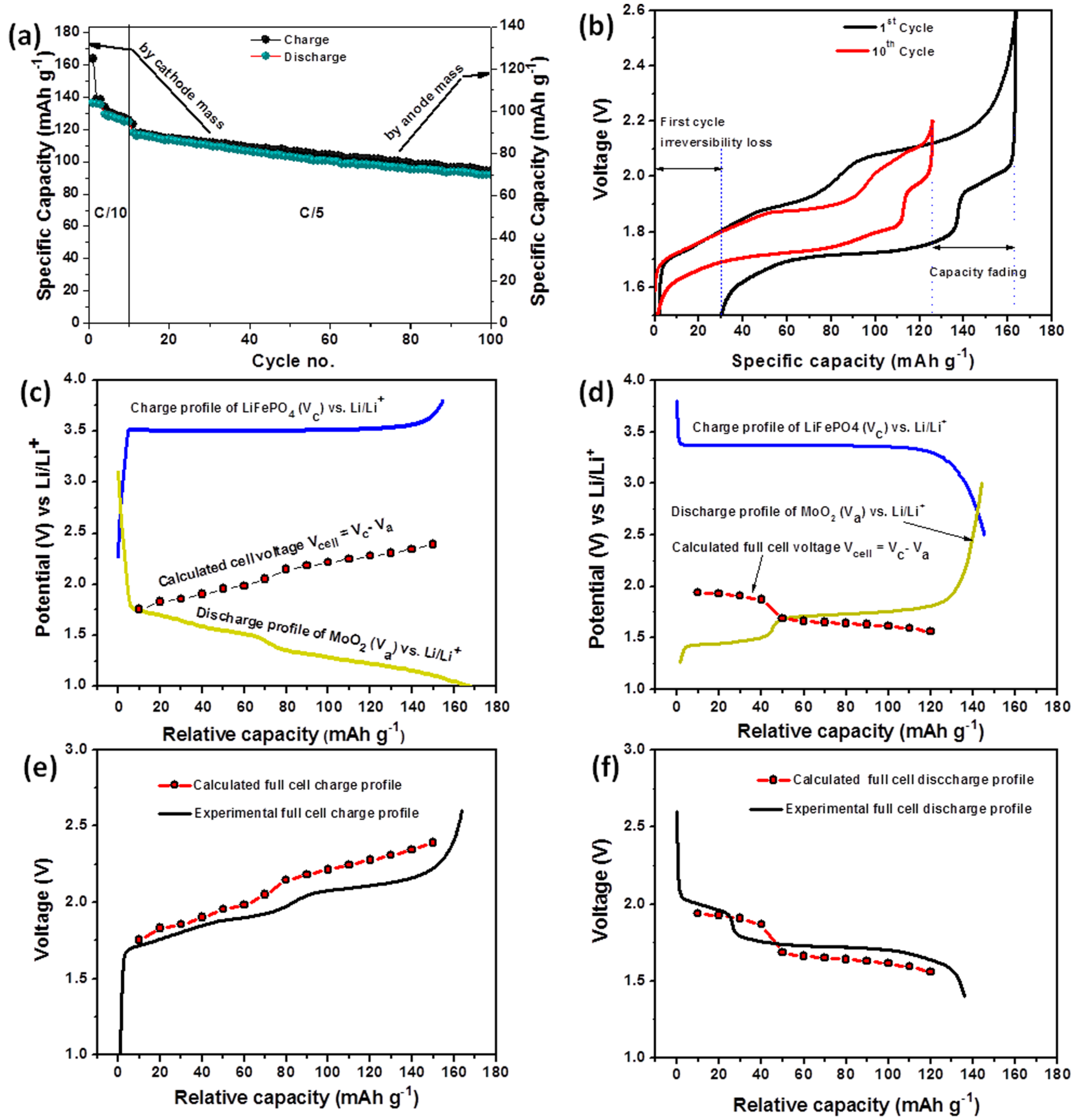

Figure 7. (a) Cyclic performance of the $LiFePO_4$/LP-30/MoO_2 full cell showing capacity normalized by the active mass of the cathode and anode and (b) the charge−discharge profile of full-cell performance using $LiFePO_4$ as cathode and MoO_2 as anode showing the 1st and the 10th cycle, (c and d) 1st cycle performance of the half-cell of $LiFePO_4$ and MoO_2 against Li/Li^+ and the calculated profile of a possible full cell. Calculated and experimental profile of full-cell charge profile (e) and discharge profile (f).

charge/discharge voltage profile of a $LiFePO_4$−MoO_2 full cell. It shows that the nature of the voltage profile is similar to what is seen in the calculated profile. An interesting observation was that the full cell unexpectedly showed lower charging and higher discharging voltage as compared to the calculated values. This may be explained by the fact that both half-cell tests were carried out in the two-electrode configuration and due to this, the polarization contribution to observed cell voltage got counted twice in the calculated profile for the full cell. This result also suggests that the contribution of the polymer separator toward cell concentration polarization was not as high as expected. However, a minor capacity fading was noted for full-cell assembly during cycling, which may be due to factors such as unstable SEI formation, lack of pressing of electrodes, cell design, and exact overlapping of electrodes. These features are not observed in half-cell characterization due to the infinite source of lithium, which replenishes any lithium loss to parasitic reactions, and the presence of an open porous structure of a comparatively thick borosilicate separator (compared to the PE separator), which allows better transport of ions across the cell and thus lower internal resistance and cell concentration polarization.

At a current density of 30 mA g^{-1}, the full cell achieved an energy density of ~70 Wh kg^{-1} at the 100th cycle. Furthermore, the present study clearly exhibits the feasibility of MoO_2 nanostructures as an excellent anode and an alternative to lithium titanate or titanium dioxide. Further work is planned to overcome issues mentioned above by means of fabrication of Li ion pouch format cells, which are better suited to study the performance of full cells.

■ CONCLUSION

In summary, for the first time MoO_2 has been focused on as an intercalation anode for lithium ion battery, and its application in a full cell has been demonstrated in this study. The nanostructured MoO_2 sample was prepared by a simple chemical conversion of MoO_3 phase. With the advantage of nanobelt morphology, which is beneficial for lithium ion and electrolyte transport, MoO_2 sample exhibits high specific capacity, good cycling stability, and excellent rate capability as an intercalation anode. A discharge capacity of 126 mAh g^{-1} was achieved at 100 mA g^{-1} after 200 cycles. Moreover, the Li ion insertion and extraction processes of MoO_2 were investigated on the basis of ex-situ X-ray diffraction and continuous electrochemical impedance spectroscopy techniques, and the phase transition reported earlier was confirmed. Finally, the Li ion cell (full cell) was successfully constructed comprising $LiFePO_4$ as cathode and MoO_2 as anode. The full cell was tested with a constant current density of 30 mA g^{-1} (C/5 with respect to $LiFePO_4$) and demonstrated an impressive performance in the initial trial. The full cell is capable of delivering a very high reversible capacity of 91 mAh g^{-1}, and the estimated energy density of 70 Wh kg^{-1} is close to that of $LiFePO_4$–$Li_4Ti_5O_{12}$ cells. The present study allows us to think beyond the current understanding and can provide a concept where MoO_2 can act as an intercalation anode within a restricted potential window. The complete cell can achieve high power performance once it is combined with a high rate cathode like $LiFePO_4$. This combination of MoO_2 anode with any high energy density cathode for full-cell fabrication can be considered as an inexpensive and safe lithium ion battery from an industrial point of view. The scalability of the cell fabrication procedures and electrode capacity balancing can be worked out further and can be easily implemented for commercial battery applications.

■ ASSOCIATED CONTENT

Supporting Information

XPS survey spectrum of a MoO_2 sample, FEG-TEM images of MoO_3 and MoO_2, and Coulombic efficiency of a MoO_2 electrode. This material is available free of charge via the Internet at http://pubs.acs.org/.

■ AUTHOR INFORMATION

Corresponding Author

*Fax: +91 22 2576 4890. Tel: +91 22 2576 7849. E-mail: sagar.mitra@iitb.ac.in.

Notes

The authors declare no competing financial interest.

■ ACKNOWLEDGMENTS

The present work is financially supported by the National Centre for Photovolatic Research and Education (NCPRE, MNRE-Govt. of India) and IRCC, IIT Bombay. Authors are thankful to the SAIF, IIT Bombay, for electron microscopy, and Central Surface Analysis Facility, IIT Bombay, for XPS analysis.

■ REFERENCES

(1) Bruce, P. G. Energy Storage Beyond the Horizon: Rechargeable Lithium Batteries. *Solid State Ionics* **2008**, *179*, 752–760.

(2) Buqa, H.; Goers, D.; Holzapfel, M.; Spahr, M. E.; Novak, P. High Rate Capability of Graphite Negative Electrodes for Lithium-Ion Batteries. *J. Electrochem. Soc.* **2005**, *152*, A474–A481.

(3) Poizot, P.; Laruelle, S.; Grugeon, S.; Dupont, L.; Tarascon, J. M. Nano-Sized Transition-Metal Oxides as Negative-Electrode Materials for Lithium-Ion Batteries. *Nature* **2000**, *407*, 496–499.

(4) Reddy, M. V.; Rao, G. V. S.; Chowdari, B. V. R. Metal Oxides and Oxysalts as Anode Materials for Li Ion Batteries. *Chem. Rev.* **2013**, *113*, 5364–5457.

(5) Etacheri, V.; Marom, R.; Elazari, R.; Salitra, G.; Aurbach, D. Challenges in the Development of Advanced Li-Ion Batteries: A Review. *Energy Environ. Sci.* **2011**, *4*, 3243–3262.

(6) Qiu, J.; Lai, C.; Gray, E.; Li, S.; Qiu, S.; Strounina, E.; Sun, C.; Zhao, H.; Zhang, S. Blue Hydrogenated Lithium Titanate as a High-Rate Anode Material for Lithium-Ion Batteries. *J. Mater. Chem. A* **2014**, *2*, 6353–6358.

(7) Dahn, J. R.; McKinnon, W. R. Structure and Electrochemistry of Li_xMoO_2. *Solid State Ionics* **1987**, *23*, 1–7.

(8) Sen, U. K.; Sarkar, S.; Veluri, P. S.; Singh, S.; Mitra, S. Nano Dimensionality: A Way towards Better Li-Ion Storage. *Nanosci. Nanotechnol. Asia* **2013**, *3*, 21–35.

(9) Veluri, P. S.; Mitra, S. Enhanced High Rate Performance of α-Fe_2O_3 Nanotubes with Alginate Binder as a Conversion Anode. *RSC Adv.* **2013**, *3*, 15132–15138.

(10) Gillot, F.; Boyanov, S.; Dupont, L.; Doublet, M. L.; Morcrette, M.; Monconduit, L.; Tarascon, J. M. Electrochemical Reactivity and Design of NiP_2 Negative Electrodes for Secondary Li-Ion Batteries. *Chem. Mater.* **2005**, *17*, 6327–6337.

(11) Sandhya, C. P.; John, B.; Gouri, C. Lithium Titanate as Anode Material for Lithium-Ion Cells: A Review. *Ionics* **2014**, *20*, 601–620.

(12) Armstrong, A. R.; Lyness, C.; Panchmatia, P. M.; Islam, M. S.; Bruce, P. G. The Lithium Intercalation Process in the Low-Voltage Lithium Battery Anode $Li_{1+x}V_{1-x}O_2$. *Nat. Mater.* **2011**, *10*, 223–229.

(13) Gonzalez, G.; Ana, M. A. S.; Benavente, E.; Donoso, J. P.; Bonagamba, T. J.; Mello, N. C.; Panepucci, H. Electrical Conductivity and Lithium Diffusion in Molybdenum Disulfide Intercalated with Poly(ethylene oxide). *Solid State Ionics* **1996**, *85*, 225–230.

(14) Shi, Y.; Guo, B.; Corr, S. A.; Shi, Q.; Hu, Y.-S.; Heier, K. R.; Chen, L.; Seshadri, R.; Stucky, G. D. Ordered Mesoporous Metallic MoO_2 Materials with Highly Reversible Lithium Storage Capacity. *Nano Lett.* **2009**, *9*, 4215–4220.

(15) Song, L. X.; Wang, M.; Pan, S. Z.; Yang, J.; Chen, J.; Yang, J. Molybdenum Oxide Nanoparticles: Preparation, Characterization, and Application in Heterogeneous Catalysis. *J. Mater. Chem.* **2011**, *21*, 7982–7989.

(16) Yao, J. N.; Yang, Y. A.; Loo, B. H. Enhancement of Photochromism and Electrochromism in MoO_3/Au and MoO_3/Pt Thin Films. *J. Phys. Chem. B* **1998**, *102*, 1856–1860.

(17) Sheehan, P. E.; Lieber, C. M. Nanotribology and Nanofabrication of MoO_3 Structures by Atomic Force Microscopy. *Science* **1996**, *272*, 1158–1161.

(18) Kim, W.-S.; Kim, H.-C.; Hong, S.-H. Gas Sensing Properties of MoO_3 Nanoparticles Synthesized by Solvothermal Method. *J. Nanopart. Res.* **2010**, *12*, 1889–1896.

(19) Sen, U. K.; Mitra, S. Electrochemical Activity of α-MoO_3 Nano-Belts as Lithium-Ion Battery Cathode. *RSC Adv.* **2012**, *2*, 11123–11131.

(20) Scanlon, D. O.; Watson, G. W.; Payne, D. J.; Atkinson, G. R.; Egdell, R. G.; Law, D. S. L. Theoretical and Experimental Study of the Electronic Structures of MoO_3 and MoO_2. *J. Phys. Chem. C* **2010**, *114*, 4636–4645.

(21) Magnéli, A.; Blomberg-Hansson, B.; Kihlborg, L.; Sundkvist, G. Studies on Molybdenum and Molybdenum Wolfram Oxides of the Homologous Series Me(*n*)O(3*n*−1). *Acta Chem. Scand.* **1955**, *9*, 1382–1390.

(22) Alves, L. M. S.; Damasceno, V. I.; dos Santos, C. A. M.; Bortolozo, A. D.; Suzuki, P. A.; Izario Filho, H. J.; Machado, A. J. S.; Fisk, Z. Unconventional Metallic Behavior and Superconductivity in the K−Mo−O System. *Phys. Rev. B* **2010**, *81*, 174532.
(23) Sun, Y.; Hu, X.; Luo, W.; Huang, Y. Self-Assembled Hierarchical MoO_2/Graphene Nanoarchitectures and Their Application as a High-Performance Anode Material for Lithium-Ion Batteries. *ACS Nano* **2011**, *5*, 7100−7107.
(24) Guo, B.; Fang, X.; Li, B.; Shi, Y.; Ouyang, C.; Hu, Y.-S.; Wang, Z.; Stucky, G. D.; Chen, L. Synthesis and Lithium Storage Mechanism of Ultrafine MoO_2 Nanorods. *Chem. Mater.* **2011**, *24*, 457−463.
(25) Ku, J. H.; Jung, Y. S.; Lee, K. T.; Kim, C. H.; Oh, S. M. Thermoelectrochemically Activated MoO_2 Powder Electrode for Lithium Secondary Batteries. *J. Electrochem. Soc.* **2009**, *156*, A688−A693.
(26) Sun, Y.; Hu, X.; Luo, W.; Huang, Y. Ultrafine MoO_2 Nanoparticles Embedded in a Carbon Matrix as a High-Capacity and Long-Life Anode for Lithium-Ion Batteries. *J. Mater. Chem.* **2012**, *22*, 425−431.
(27) Xu, Y.; Yi, R.; Yuan, B.; Wu, X.; Dunwell, M.; Lin, Q.; Fei, L.; Deng, S.; Andersen, P.; Wang, D.; Luo, H. High Capacity MoO_2/Graphite Oxide Composite Anode for Lithium-Ion Batteries. *J. Phys. Chem. Lett.* **2012**, *3*, 309−314.
(28) Xia, F.; Hu, X.; Sun, Y.; Luo, W.; Huang, Y. Layer-by-Layer Assembled MoO_2−Graphene Thin Film as a High-Capacity and Binder-Free Anode for Lithium-Ion Batteries. *Nanoscale* **2012**, *4*, 4707−4711.
(29) Sun, Y.; Hu, X.; Yu, J. C.; Li, Q.; Luo, W.; Yuan, L.; Zhang, W.; Huang, Y. Morphosynthesis of a Hierarchical MoO_2 Nanoarchitecture as a Binder-Free Anode for Lithium-Ion Batteries. *Energy Environ. Sci.* **2011**, *4*, 2870−2877.
(30) Werfel, F.; Minni, E. Photoemission Study of the Electronic Structure of Mo and Mo oxides. *J. Phys. C: Solid State Phys.* **1983**, *16*, 6091−6100.
(31) Sarkar, S.; Veluri, P. S.; Mitra, S. Morphology Controlled Synthesis of Layered $NH_4V_4O_{10}$ and the Impact of Binder on Stable High Rate Electrochemical Performance. *Electrochim. Acta* **2014**, *132*, 448−456.
(32) Aurbach, D.; Markovsky, B.; Weissman, I.; Levi, E.; Ein-Eli, Y. On the Correlation Between Surface Chemistry and Performance of Graphite Negative Electrodes for Li Ion Batteries. *Electrochim. Acta* **1999**, *45*, 67−86.
(33) Aurbach, D.; Gamolsky, K.; Markovsky, B.; Salitra, G.; Gofer, Y.; Heider, U.; Oesten, R.; Schmidt, M. The Study of Surface Phenomena Related to Electrochemical Lithium Intercalation into Li_xMO_y Host Materials (M = Ni, Mn). *J. Electrochem. Soc.* **2000**, *147*, 1322−1331.
(34) Qiu, X.-Y.; Zhuang, Q.-C.; Zhang, Q.-Q.; Cao, R.; Ying, P.-Z.; Qiang, Y.-H.; Sun, S.-G. Electrochemical and Electronic Properties of $LiCoO_2$ Cathode Investigated by Galvanostatic Cycling and EIS. *Phys. Chem. Chem. Phys.* **2012**, *14*, 2617−2630.
(35) Ruffo, R.; Hong, S. S.; Chan, C. K.; Huggins, R. A.; Cui, Y. Impedance Analysis of Silicon Nanowire Lithium ion Battery Anodes. *J. Phys. Chem. C* **2009**, *113*, 11390−11398.
(36) Zhu, J. G.; Sun, Z. C.; Wei, X. Z.; Dai, H. F. A New Electrochemical Impedance Spectroscopy Model of a High-Power Lithium-Ion Battery. *RSC Adv.* **2014**, *4*, 29988−29998.
(37) Reddy, M. V.; Prithvi, G.; Loh, K. P.; Chowdari, B. V. R. Li Storage and Impedance Spectroscopy Studies on Co_3O_4, CoO, and CoN for Li-Ion Batteries. *ACS Appl. Mater. Interfaces* **2013**, *6*, 680−690.
(38) Wang, G.; Yang, L.; Chen, Y.; Wang, J.; Bewlay, S.; Liu, H. An Investigation of Polypyrrole−$LiFePO_4$ Composite Cathode Materials for Lithium-Ion Batteries. *Electrochim. Acta* **2005**, *50*, 4649−4654.
(39) Nobili, F.; Croce, F.; Scrosati, B.; Marassi, R. Electronic and Electrochemical Properties of $Li_xNi_{1-y}Co_yO_2$ Cathodes Studied by Impedance Spectroscopy. *Chem. Mater.* **2001**, *13*, 1642−1646.
(40) Nobili, F.; Tossici, R.; Marassi, R.; Croce, F.; Scrosati, B. An AC Impedance Spectroscopic Study of Li_xCoO_2 at Different Temperatures. *J. Phys. Chem. B* **2002**, *106*, 3909−3915.
(41) Nobili, F.; Dsoke, S.; Minicucci, M.; Croce, F.; Marassi, R. Correlation of Ac-Impedance and In Situ X-ray Spectra of $LiCoO_2$. *J. Phys. Chem. B* **2006**, *110*, 11310−11313.